Astronomy & Astrophysics manuscript no. jekyll
February 20, 2018
©ESO 2018

Monte-Carlo methods for NLTE spectral synthesis of Supernovae.

M. Ergon[1], C. Fransson[1], A. Jerkstrand[2], C. Kozma[1], and M. Kromer[3,4]

[1] The Oskar Klein Centre, Department of Astronomy, AlbaNova, Stockholm University, 106 91 Stockholm, Sweden
[2] Max-Planck-Institut für Astrophysik, Karl-Schwarzschild-Str. 1, D-85748 Garching, Germany
[3] Heidelberger Institut für Theoretische Studien, Schloss-Wolfsbrunnenweg 35, D-69118 Heidelberg, Germany
[4] Institut für Theoretische Astrophysik am Zentrum für Astronomie der Universität Heidelberg, Philosophenweg 12, D-69120 Heidelberg, Germany

To be submitted to Astronomy and Astrophysics.

ABSTRACT

We present JEKYLL, a new code for modelling of SN spectra and lightcurves based on Monte-Carlo (MC) techniques for the radiative transfer. The code assumes spherical symmetry, homologous expansion and steady state for the matter, but is otherwise capable of solving the time-dependent radiative transfer problem in non-local-thermodynamic-equilibrium (NLTE). The method used was introduced in a series of papers by **Lucy, but the full time-dependent NLTE capabilities of it have never been tested. Here**, we have extended it to include non-thermal excitation and ionization as well as charge-transfer and two-photon processes. Based on earlier work, we calculate the non-thermal rates by solving the Spencer-Fano equation, and the macroscopic mixing of the material, known to occur in the SN explosion, **is taken into account in a statistical sense**. To save computational power we use a **diffusion solver** in the inner region, where the radiation field **may be assumed to be** thermalized. **In addition, we use Markov-Chains to sample the emission frequency more efficiently, and introduce a method to control the sampling of the radiation field, which is used to reduce the noise in the radiation field estimators.** Except for a description of JEKYLL, we provide comparisons with the ARTIS, **SUMO and CMFGEN codes, which show** good agreement in the calculated spectra as well as the state of the gas. **In particular, the comparison with CMFGEN, which is similar in terms of physics but use a different technique, shows that the Lucy method does indeed converge in the time-dependent NLTE case. Finally, as an example of the time-dependent NLTE capabilities of JEKYLL we present a model of a Type IIb SN, taken from a set of models presented and discussed in detail in an accompanying paper. Based on this model we investigate the effects of NLTE by switching it off, and find strong effects even on the bolometric lightcurve. This highlights the need for full NLTE calculations when simulating the spectra and lightcurves of SNe.**

Key words. supernovae: general

1. Introduction

Modelling the spectral evolution and lightcurves of supernovae (SNe) is crucial for our understanding of these phenomena, and much effort has been put into this during the last 50 years. To achieve realistic results local thermodynamic equilibrium (LTE) can generally not be assumed, and the full frequency-dependent, non-LTE (NLTE) problem has to be solved. Several paths exist and here we follow the one outlined in a series of papers by Lucy (2002, 2003, 2005, hereafter L02, L03, L05), **in turn based on earlier work by Mazzali & Lucy (1993) and Lucy (1999)**. Using this method, **hereafter referred to as the Lucy method**, the radiative transfer is solved by a Monte-Carlo (MC) calculation, which is alternated with a NLTE solution for the matter until convergence is achieved (Λ-iteration). Basic tests were performed in the original papers, and a simplified version of the method, assuming LTE for the population of excited states, has been implemented in the code ARTIS (Kromer & Sim 2009, hereafter K09). Several other codes, as e.g. TARDIS (Kerzendorf & Sim 2014), SEDONA (Kasen et al. 2006), **SAMURAI (Tanaka et al. 2007) and the one by Mazzali (2000)** are also based on the method, **(or the early version of it)**, **but are all restricted to LTE, steady-state or both.** Here we present JEKYLL, a C++ based code which implements the full NLTE-version of the method, extended to include also non-thermal excitation and ionization as well as charge-transfer and two-photon processes. These extensions are particularly important for modelling in the nebular phase, and for the calculation of the non-thermal rates we use the method developed by Kozma & Fransson (1992, hereafter KF92). Contrary to ARTIS, the initial version of JEKYLL is restricted to a spherical symmetric geometry, although the MC radiative transfer is performed in 3-D. **Another code based on Λ-iteration and MC radiative transfer is** the steady-state **NLTE** code SUMO **(Jerkstrand et al. 2011, 2012, hereafter J11,J12)** aimed for the nebular phase, **although the MC technique is different**. **SUMO uses a statistical approach to represent the macroscopic mixing of the ejecta occurring in the explosion, which we have adopted in JEKYLL. In addition to the MC based codes, there is a group of codes that use finite difference techniques to solve the radiative transfer equation in a more traditional way. Examples of such codes are PHOENIX (Hauschildt & Baron 1999) and** the general purpose NLTE code CMFGEN (Hillier & Miller 1998, hereafter H98), **which is similar to JEKYLL in terms of physics**. In this paper, **we compare JEKYLL with CMFGEN as well as with ARTIS and SUMO, which are also similar to JEKYLL in one way or another. These comparisons** provide a **thorough and** critical test of the **JEKYLL code**. **In a broader context, the comparison with CMFGEN also provide a test of the full time-dependent NLTE capabilities of the Lucy method.**

In an accompanying paper (Ergon et al. in prep, hereafter Paper 2) we present an application of JEKYLL to Type IIb SNe, by modelling the early evolution of a set of Type IIb models previously evolved through the nebular phase (J15). Out of those, one model is presented in this paper as an example of a time-dependent NLTE calculation using a realistic ejecta model. However, for comparisons to observations and a deeper discussion of Type IIb SNe we refer to Paper 2.

The paper is organized as follows. In Sect. 2 we discuss the underlying physical problem, and in Sect. 3 we describe the method used to solve this problem and the design of the code. In Sect. 4 we provide **the** comparisons of **JEKYLL with the ARTIS**, **SUMO and CMFGEN codes, and in Sect. 5 we provide the example application.** Finally, in Sect. 6 we conclude and summarize the paper.

2. Physics

The general physical problem **addressed** is the time-evolution of the radiation field and the state of the matter, given the dynamical constraint of homologous expansion, and might be referred to as a radiation-thermodynamical problem. If the radiation field and the matter are in local thermodynamic equilibrium (LTE) this is simplified to a one-parameter (i.e the temperature) problem, and may be easily solved. Otherwise, we are in the non-LTE (NLTE) regime, and the number of parameters, as well as the complexity of the problem, increase drastically.

As is often done, we solve for the radiation field and state of the matter separately, and the problem is split into a radiative transfer and a thermodynamical part. The coupling, provided by radiation-matter interactions, is enforced through Λ-iterations, where the state of the matter and the radiation field are alternately and iteratively determined from each other. The Λ-iteration concept is at the heart of the method, and in Sect. 2.1 we provide some background and discuss the somewhat different meaning it has in traditional and MC based methods.

The state of the matter can be separated into a dynamical and thermodynamical part, where the former is trivially given by $\rho = \rho_0\,(t/t_0)^{-3}$ and $v = r/t$ through the constraint of homologous expansion. The thermodynamical part is given by the temperature, and the populations of ionized and excited states, which are solved for using the thermal energy equation and the NLTE rate equations, respectively. To simplify we assume steady state, which is motivated if the thermodynamical time-scale is much smaller than the dynamical time-scale.

The radiation field is given by the specific intensity, which is solved for using **an extended version of the MC based Lucy method, which is** discussed in Sect. 3.3. In a traditional code like CMFGEN, the specific intensity is solved for using the radiative transfer equation, whereas in a MC based code like JEKYLL, the radiative transfer is treated explicitly by propagating radiation packets which interact with the matter through absorption, emission and scattering. The different radiation-matter interactions supported are discussed in Sect. 2.4.

In addition, radioactive decays emit high-energy photons or leptons, which give rise to a non-thermal electron distribution. Through collisions, these electrons contribute to the heating of the electron gas and the excitation and ionization of the ions. The problem may be broken up into two parts; deposition of the radioactive decay energy, and the partitioning of this energy into non-thermal heating, ionization and excitation.

2.1. Λ-iterations and convergence

In terms of the Λ-operator the radiative transfer equation may be written as $I = \Lambda[S]$, where I is the intensity and S the source-function. If the source function depends on the intensity, as in the case of scattering, solving the problem requires inverting the Λ-operator. This is typically a costly operation, and we may instead try an iterative procedure called Λ-iteration (see e.g. Hubeny & Mihalas 2014). In its original form an improved estimate of the intensity is then determined using the previous estimate of the source-function, i.e. $I_{i+1} = \Lambda[S_i]$. However, this method may converge extremely slowly if the source function is dominated by scattering, as the non-local coupling introduced only propagates one mean-free path per iteration. This may be solved by splitting the Λ-operator in two parts, one acting on the current iteration and one acting on the previous iteration, i.e. $I_{i+1} = \Lambda^*[S_{i+1}] + (\Lambda - \Lambda^*)[S_i]$. With an appropriate choice of Λ^*, e.g the local part of Λ, which is trivial to invert and still close to Λ, convergence could be accelerated, and the procedure is therefore known as accelerated Λ-iteration (see e.g. **Cannon 1973b,a**, Scharmer 1984, Werner & Husfeld 1985 and Olson et al. 1986).

It is important to realize that **the explicit dependence of the scattering emissivity on the intensity does not cause slow convergence in the MC case.** The reason for this is that the MC scattering emissivity depends directly on the current iteration of the MC radiation field. Actually, **a MC** Λ-iteration is **similar** to an accelerated Λ-iteration **in the sense that the current iteration depends partly on itself. Note, however, that the implicit dependence of the MC emissivities on the intensity (via the matter quantities) may still cause slow convergence, and this is the problem addressed by the Lucy method.** Enforcing the constraints of thermal and statistical equilibrium on the MC calculation, introduces a direct (but approximate) dependence of all MC emissivities on the current iteration of the MC radiation field. **Although not formally proved, this is likely to accelerate the convergence in the general case**, and as demonstrated in L03, Λ-iterations based on this **method** have excellent convergence properties.

2.2. Statistical equilibrium

To determine the populations of ionized and excited states, the NLTE rate equations need to be solved. Assuming steady state, these equations simplify to the equations of statistical equilibrium, where the rates of transitions in and out of each state are in equilibrium. The statistical equilibrium equation for level i of ion I may be written

$$\sum_{J=I\pm1} r^{\mathrm{BF}}_{J,j\rightarrow I,i}\, n_{J,j} + \sum_{j\neq i} r^{\mathrm{BB}}_{I,j\rightarrow i}\, n_{I,j} = \left(\sum_{J=I\pm1} r^{\mathrm{BF}}_{I,i\rightarrow J,j} + \sum_{j\neq i} r^{\mathrm{BB}}_{I,i\rightarrow j} \right) n_{I,i} \tag{1}$$

where r is **the rate** (per particle) for bound-free (superscript BF) and bound-bound (superscript BB) transitions, and n is the number density. **Note that the system of equations is non-linear as (some) transition rates (per particle) depends on the number densities.** Transitions may be caused by absorption/emission of photons (Sect. 2.4), or by collisions involving ions and thermal (Sect. 2.5) or non-thermal (Sect 2.6.1) electrons.

2.3. Thermal equilibrium

To determine the thermal state of the gas the thermal energy equation needs to be solved. Assuming steady state, this equa-

tion simplifies to the equation of thermal equilibrium, where the heating and cooling of the gas are in equilibrium. The thermal equilibrium equation may be written

$$\sum_{J=I\pm1} g^{\mathrm{BF}}_{I,i\rightarrow J,j}(T)\, n_{I,i} + \sum_{i\neq j} g^{\mathrm{BB}}_{I,i\rightarrow j}(T)\, n_{I,i} + \sum g^{\mathrm{FF}}_{I}(T)\, n_{I,i} = H^{\mathrm{NT}} \quad (2)$$

where g is the net heating rate (per particle) for bound-free (superscript BF), bound-bound (superscript BB) and free-free (superscript FF) transitions, and H^{NT} is the heating rate by non-thermal collisions. Heating/cooling may arise through absorption/emission of photons (Sect. 2.4), or through collisions involving ions and thermal (Sect. 2.5) or non-thermal (Sect 2.6.1) electrons.

2.4. Radiation-matter interactions

In radiation-matter interactions, the radiation field and the matter (electrons and ions) exchange energy through absorption and emission of photons. Except for electron scattering, which is assumed to be coherent and isotropic in the co-moving frame (of the ejecta), and given by the Thomson cross-section, JEKYLL supports the following interactions.

Bound-bound Through detailed balance, the excitation and de-excitation rates are related and determined by a single quantity, e.g. the spontaneous emission coefficient. We assume that the Sobolev approximation **(Sobolev 1957)** applies, which is appropriate when expansion broadening dominates **the thermal broadening**. Expressions for the Sobolev optical depth as well as the transition rates are given in L02. In addition, we also support de-excitation through two-photon emission for bound-bound transitions otherwise radiatively forbidden.

Bound-free Through detailed balance, the ionization and recombination rates are related and determined by a single quantity, e.g. the photo-ionization cross-section. In bound-free transitions, the energy absorbed/emitted goes partly into ionization/recombination of the ion, and partly into heating/cooling of the electron gas. Expressions for the opacity, emissivity, transition rates and heating/cooling rates are given in L03.

Free-free **(i.e. bremsstrahlung)** Assuming thermal matter, the opacity and emissivity are related through Kirchoffs law. In free-free interactions, the energy of the photons absorbed/emitted goes solely into heating/cooling of the electron gas. Expressions for the opacity, emissivity, and heating/cooling rates are given in L03.

2.5. Matter-matter interactions

In matter-matter interactions, electrons and ions exchange energy through collisions. The collisions heat/cool the electron gas and result in bound-bound or bound-free transitions of the ions. Except for non-thermal collisions, which are discussed in Sect. 2.6.2, JEKYLL supports the following interactions.

Bound-bound and bound-free Through detailed balance, the collisional excitation and de-excitation rates are related and determined by a single quantity, e.g. the collisional strength. The same is true for the collisional ionization and recombination rates, and expressions for the transition rates and heating/cooling rates are given in L03.

Charge-transfer In collisions involving two ions, electrons may be transferred from one ion to another. This process is called charge-transfer and may be viewed as a recombination followed by a ionization. The charge transfer rates may be expressed in terms of a charge-transfer coefficient (α) that depends only on the temperature as

$$\begin{aligned} R_{\bar{I},\bar{J}\rightarrow\bar{U},\bar{L}} &= \alpha_{\bar{I},\bar{J}\rightarrow\bar{U},\bar{L}}(T)\, n_{\bar{I}}\, n_{\bar{J}} \\ R_{\bar{U},\bar{L}\rightarrow\bar{I},\bar{J}} &= \frac{\alpha_{\bar{I},\bar{J}\rightarrow\bar{U},\bar{L}}(T)}{\phi_{\bar{I},\bar{J},\bar{U},\bar{L}}(T)}\, n_{\bar{U}}\, n_{\bar{L}} \end{aligned} \quad (3)$$

where $\phi_{\bar{I},\bar{J},\bar{U},\bar{L}}(T) = (n^*_{\bar{I}}\, n^*_{\bar{J}})/(n^*_{\bar{U}}\, n^*_{\bar{L}})$, the asterisk indicates the LTE value and $\bar{I} = (I, i)$ is an index vector specifying **level i of ion I**. The energy difference between the initial and final state of the process gives rise to heating or cooling of the electron gas with a rate given by $R_{\bar{I},\bar{J}\rightarrow\bar{U},\bar{L}}\ \left|\chi_{\bar{I},\bar{U}} - \chi_{\bar{L},\bar{J}}\right|$, where χ is the ionization energy.

2.6. Radioactive decays

2.6.1. Energy deposition

The energy released in the radioactive decays is carried by high-energy photons and leptons which deposit their energy in the ejecta mainly through Compton scattering on free and bound electrons. Although a detailed calculation is preferred, we use effective grey opacities determined through such calculations. We **support the** decay chains ^{56}Ni $\rightarrow$ ^{56}Co $\rightarrow$ ^{56}Fe, ^{57}Ni $\rightarrow$ ^{57}Co $\rightarrow$ ^{57}Fe and ^{44}Ti $\rightarrow$ ^{44}Sc $\rightarrow$ ^{44}Ca, which are the most important for core-collapse SNe. For these decays we adopt the life-times and **energies** from Kozma & Fransson (1998) and the effective grey γ-ray opacities from J11, and assume that the positrons emitted are locally absorbed.

2.6.2. Energy partition

Through a cascade of collisions the deposited energy gives rise to a high-energy tail on the otherwise Maxwellian electron distribution. The shape of the non-thermal electron distribution and the fractions of the energy going into heating, excitation and ionization through non-thermal collisions can be calculated by solving the Spencer-Fano equation (Boltzman equation for electrons). This problem was solved by KF92 and for a further discussion we refer to this paper.

3. Method and design

Given the physical problem, we now describe the methods used to solve it, and provide an outline of how the code is designed. Except for the non-thermal solver, the code is written in C++, and the description therefore tends to reflect the object oriented structure of the code. The code is parallelized on a hybrid process (MPI) and thread **(openMP)** level.

The SN ejecta **are** represented by a spatial grid of cells holding the local state of the matter and the radiation field. Although mostly geometry independent, the current version only supports spherically symmetric cells. To determine the state of the matter, JEKYLL provides several solvers with different levels of approximation (e.g. LTE and NLTE), and to determine the radiation field it provides a MC solver based on the **Lucy method**. As

discussed, through Λ-iterations the matter and the radiation field are alternately determined from each other, a procedure which in JEKYLL is terminated after a fixed but configurable number of iterations. JEKYLL also provides a diffusion solver, intended for use at high optical depths where the matter and radiation field may be assumed to be in LTE. JEKYLL may be configured to run in steady-state or time-dependent mode, although the latter only applies to the radiative transfer. Steady-state **for the radiation field** breaks down if the diffusion time is large, and is therefore best suited for modelling in the nebular (optically thin) phase, or of the SN atmosphere in the photospheric (optically thick) phase.

3.1. Grid

The grid represents the SN ejecta and is spatially divided into a number of cells, which in the current version of the code are spherically symmetric. **As mentioned, the code is mostly geometry independent, so cells with other geometries may easily be added in future versions of it.** If macroscopic mixing is used, the cells may be further divided into compositional zones, geometrically realized as virtual cells. The grid provides functions to load the ejecta model, to load and save the state, as well as to export a broad range of derived quantities (e.g. opacities).

3.1.1. Cells

The cells hold the local state of the matter and the radiation field, and provide functions for the solvers to calculate derived quantities like opacities/emissivities and transition rates based on the local state and the atomic data. The local state of the matter is represented by the density, the temperature, and the number fractions of ionized and excited states. The local state of the radiation field is represented by the specific intensity, which is updated by the MC radiative transfer solver based on packet statistics following the method outlined by L03. In addition, JEKYLL supports simplified radiation field models based on pure or diluted blackbody radiation, given by $B_\nu(T_J)$ and $WB_\nu(T_R)$, respectively (see K09 for details). **JEKYLL also allows the radiation-field to be approximated by the source-function as $I = S(\mathbf{n}, T)$, which depends only on the local state of the matter. This option** is intended for use **bluewards ground-state ionization edges**, which typically have high optical depths and dominate the source-function. **When using this approximation, we only include bound-free opacities and emissivities in the source function, which is likely a good approximation.**

3.1.2. Virtual cells

JEKYLL implements the concept of virtual cells, introduced by J11 to account for macroscopic mixing on a grid otherwise spherically symmetric. Each cell may be divided into zones occupying some fraction (filling factor) of the cell volume, and otherwise geometrically unspecified. These zones may have different densities and compositions, and the state is solved for separately by the matter-state solver. With respect to the MC-solver the zones are represented by virtual cells differing only in a geometrical and statistical sense. The virtual cells are spherical, have a size corresponding to some number of clumps, and their location is randomly drawn during the MC radiative transfer based on their size and the zone filling factor.

3.2. Atomic data

Once converted to the JEKYLL format, any set of atomic data may be loaded from file. The data is organized in a hierarchical structure of atoms, their isotopes and ions, and the bound states of the ions. Each ion holds a list of bound-bound transitions, and each atom holds a list of bound-free transitions. The atomic data also contains an (optional) list of charge-transfer reactions, which are mapped on two bound-free transitions, one recombination and one ionization. The specific atomic data used for the comparisons in Sects. 4.1-4.3 are discussed in Appendix A.1-A.3. **The default choice, used for the application in Sect. 5, is inherrited from SUMO (see J11 and J12), and have been extended as described in Appendix A.4.**

3.3. MC radiative transfer solver

The MC radiative transfer solver determines the radiation field, and is based on the **Lucy method**. The radiation field is discretized as packets (Sect. 3.3.1), which are propagated on the grid (Sect. 3.3.2) and interact with the matter (Sect. 3.3.3). **Note, that the packets are propagated in 3-D, so the constraint of spherical symmetry only applies to the grid they are propagated on.** In the calculation, the constraints of statistical and thermal equilibrium are enforced, which accelerates the convergence of the Λ-iterations (see Sect.2.1). The **original** method has been extended to include non-thermal ionizations and excitations, as well as charge-transfer and two-photon processes. In addition, we introduce an alternative, more efficient way to draw the emission frequency (Sect. 3.3.4), and a method to control the sampling of the radiation field (Sect. 3.3.4). Although we explain the basics, we refer to L02-L05 for the details of the original method.

3.3.1. Packets

The radiation field is discretized as packets, defined by their energy, frequency, position and direction. Following L03 and K09, we classify these as r-, i-, k- and γ-packets. The packets are indivisible and indestructible (but see Sect. 3.3.4 for a modified requirement), which enforce the constraint of thermal equilibrium on the MC calculation. Freely propagating photons are represented by r-packets, and upon absorption they are converted into i- and k-packets, representing ionization/excitation and thermal energy, respectively. The γ-packets are similar to the r-packets, but represent the γ-rays (or leptons) emitted in the radioactive decays, which are treated separately. Eventually, the i- and k-packets are converted into r-packets and re-emitted.

New r-packets are injected into the MC-calculation by sampling of the **flux** at the inner border (if any), and new γ-packets by sampling of the γ-ray emissivity. In addition, r-packets may be sampled from the **initial** intensity in each cell, as well as from **the intensity in** new cells taken over from the diffusion solver when the inner border is moved inwards.

3.3.2. Propagation

When the r- and γ-packets are propagated they undergo physical (radiation-matter interactions) and geometrical (border crossings) events. Whereas propagation is carried out in the rest frame, the physical events take place in the co-moving frame, and the packets are transformed back and forth to $O(v/c)$. After each event, a random optical depth for the next physical event is drawn as $\tau = -\ln z$, and the packet is propagated until the

accumulated optical depth exceeds this value or a geometrical event occurs. Note that line-absorption may only occur at the resonance distances, and the (Sobolev) line-opacity may be regarded as a delta-function. In the case of a physical event, the packet is processed as described in Sect. 3.3.3, and in either case propagation continues as described above. Note, that in the case of γ-packets we use effective grey opacities (Sect 2.6.2), which differs from the more detailed procedure by L05. The r- and γ-packets leave the MC calculation by escaping through the outer border, where the r-packets are binned and summed to build the observed spectrum. **When doing this we take light-travel time into account by defining the observers time as $t_O = t-(R/c)\mu$, where R is the radius of the grid and μ the cosine of the angle between the packet direction and the radius vector.**

If the packet enters a cell divided into compositional zones (Sect. 3.1.2), a randomly oriented virtual cell is drawn based on the filling factor of the corresponding zone **(see J11 for details)**. As long as the packet remains in the cell, the distance to the next geometrical event is given by the size and the orientation of the virtual cell, and at each (virtual) border crossing the procedure is repeated.

3.3.3. Interactions

Once the packet has been absorbed, the type of interaction is drawn in proportion to the opacities. In the case of electron scattering, the frequency does not change. Otherwise, an emission frequency is drawn as described by L02 and L03, which enforces the constraints of statistical and thermal equilibrium on the MC calculation. Below we provide a summary of the **original** method and describe the extensions made for non-thermal, charge-transfer and two-photon processes. Before re-emission of the packet a new direction is drawn from an isotropic distribution.

Original method To enforce the aforementioned constraints on the MC calculation, L02 and L03 introduce the concepts of macro-atoms and the thermal pool, which are the MC analogues of the statistical and thermal equilibrium equations. The macro-atoms are state-machines mirroring the energy structure of the atomic species, and are activated by upward transitions (e.g. excitations) and de-activated by downward transitions (e.g. de-excitations). In de-activations through radiative transitions, i-packets are converted to r-packets and re-emitted, whereas in de-activations through collisional transitions, i-packets are converted to k-packets and transferred to the thermal pool. The k-packets enter the thermal pool through radiative and collisional heating and leave through radiative and collisional cooling, in which case they are converted into r- or i-packets in proportion to the cooling rates. Together, the macro-atoms and the thermal pool constitute a single state-machine activated by an absorption of a r- or γ-packet, and de-activated by the emission of **an** r-packet. The absorbed r- and γ-packets are converted into i- or k-packets in proportion to the energy going into ionization/excitation and heating. The frequency of the emitted r-packet is drawn from the (normalized) emissivity of the de-activating process.

Although the method is conceptually simple, it is a bit involved in the details, not the least with respect to the macro-atoms. These are activated either by radiative or collisional upward transitions (e.g. excitations), drawn in proportion to their opacities and cooling rates, respectively. If a macro-atom is activated at level i, each physical transition with number rate $R_{i,j}$ corresponds to an internal state-machine transition with probability $p_{i,j} \propto R_{i,j}E_l$ (L02: Eq. 9), where E_l is the energy of level $l = min(i, j)$. In addition, each physical downward transition (e.g. de-excitation) may de-activate the macro-atom with probability $p_{i,l} \propto R_{i,l}(E_i - E_l)$ (L02: Eq. 7). If an internal transition is drawn the state-machine proceeds to level j and the procedure is repeated.

Non-thermal processes Upon absorption, γ-packets are converted into i- or k-packets in proportion to the energy going into ionization/excitation and heating. This differs from the original method where only the heating channel was allowed. In the case of an i-packet, a macro-atom state-machine is activated by a non-thermal transition drawn in proportion to its energy rate. The macro-atom state-machines are modified by adding the probabilities for non-thermal transitions calculated from their number rates as explained above. Non-thermal transitions are upward, and therefore correspond to internal transitions.

Charge-transfer processes As mentioned, charge-transfer is a collisional process that may be viewed as a recombination followed by an ionization, where the (small) energy difference results in either heating or cooling. The macro-atom state-machines are therefore modified by adding the probabilities for the corresponding ionizations and recombinations calculated from their number rates as explained above. Charge-transfer ionizations correspond to internal transitions, whereas charge-transfer recombinations correspond to internal and de-activating transitions.

De-activation of a macro-atom state-machine through a charge-transfer recombination results in either activation of another macro-atom state-machine through the corresponding ionization or in the conversion of the i-packet into a k-packet. The latter corresponds to the conversion of ionization energy into thermal energy, may only happen if the reaction is exo-thermic, and is drawn in proportion to the energy going into heating. Correspondingly, if the reaction is endo-thermic, k-packets may be converted into i-packets, and a macro-atom state-machine activated by the corresponding ionization. This corresponds to the conversion of thermal energy into ionization energy, and is drawn in proportion to the cooling rate as described above.

Two-photon processes The macro-atom state-machines are modified by adding the probabilities for two-photon transitions calculated from their number rates as explained above. Two-photon transitions are downward, and might therefore be either internal or de-activating, and in the latter case the emission frequency is drawn from the (normalized) two-photon emissivity.

3.3.4. Markov-chain solution to the state-machine

A problem with the original method is that the number of transitions in the state-machine may become very large. This is particularly true when the collisional rates are high, causing the state-machine to bounce back and forth between macro-atoms and the thermal pool. To avoid this we use **a statistical Markov-chain model** to calculate the probability that the state-machine **de-activates from a given state**. This approach can be applied **to** individual macro-atoms, or to the complete state-machine. According to Markov-chain theory (see e.g. Ross 2007), the average **number of times** spent in state i, given that the machine is invoked in state j, **is** specified by the matrix $S_{i,j}$. **This matrix**

can be calculated from the matrix $P_{i,j}$, containing the probabilities for internal transitions from state i to state j, through the relation $S^{-1} = P - I$, **where I is the identity matrix**. **The probability that the machine de-activates from state i is proportional to the average number of times spent in this state, and is therefore given by the (row-normalized) S matrix. Once we have calculated S, we do not need to walk through the state-machine each time it is invoked, but may instead draw the state from which it de-activates, and proceed to it directly. Once in this state**, we **just** draw the de-activating transition from their (normalized) probabilities. **The implementation is based on** two look-up tables for each state, one containing (a **normalized** row of) S, and one containing the (normalized) de-activating transition probabilities. **The procedure is now very simple, the de-activating state is drawn from the former table, the state-machine proceeds to this state, and the de-activating transition is drawn from the latter table.**

Applying the method to individual macro-atoms, the states, the internal transitions and the de-activating transitions are the same a described in L02. Applying the method to the complete state-machine, the states are those of all macro-atoms and the thermal pool. In this case, collisional activation and de-activation of the macro-atoms correspond to internal transitions between the thermal pool and the macro-atoms. Applying the method to the complete state-machine, the S matrix has size $N \times N$, where N is the total number of energy levels for all **macro-atoms** plus one (the thermal pool), and the computational time to invert the matrix is a potential problem. This may be circumvented by splitting the state-machine into top-level and **macro-atom** parts, and calculate the corresponding S-matrices separately. The procedure is similar to what is described above, but the computational time to invert the top-level and **macro-atom** S-matrices is much less than for the complete S-matrix. **We give the details on the split state-machine approach in Appendix A.5.**

3.3.5. Packet sampling control

Another problem with the original method is that there is no (or limited) control of the number of packets as a function of frequency, space and time. This may result in too few packets, leading to noise in the radiation field estimators, or too many, leading to unnecessary computational effort. **The number of packets can not be directly controlled, but this might instead be achieved by adjusting their size, i.e. their energy. By conservation of quantity (energy) the number of packets is inversely proportional to their size (energy). We therefore** introduce a method for continuous re-sampling of the radiation field **through control of the packet size (energy), which is allowed to** vary as a function **of** frequency, space and time. This breaks the indivisibility and destructibility requirements introduced by L02, but conservation of energy, **which is the essential property**, is still maintained in an average sense.

A set of sampling regions (bounded in frequency, space and time) is defined, and each of these is assigned a packet **size (energy)**. When packets cross the borders between sampling regions, their **size (energy)** is adjusted to that of the destination region. To maintain the rate of energy flowing across the borders, the rate of packets flowing across the borders has to be adjusted with the ratio **(F)** of the packet **sizes (energies)** in the source and destination regions. **When borders are crossed due to propagation, this is achieved by splitting the packets into F child packets (if F>1) or terminating them with probability 1-F (if F<1). When (frequency) borders are crossed due to interactions with the matter**, this is achieved by adjusting the emission rates **(in terms of packets)** with F. **However, this means that also the interaction rate needs to be adjusted, and therefore we introduce** a fictitious opacity (κ_F) corresponding to the total adjusted emission rate (which may be higher or lower than the original one). Although the basic idea is **straightforward**, the actual implementation is complicated by the way the emission frequency is drawn (Sect. 3.3.3).

Replacing κ with $max(\kappa, \kappa_F)$, packets are selected for either absorption, emission or both. The packet is absorbed with probability $max(\kappa/\kappa_F, 1)$ and emitted with probability $max(\kappa_F/\kappa, 1)$. If the packet is absorbed but not emitted it is terminated, and if the packet is emitted but not absorbed a child packet is created. Otherwise the transition is handled as described above (which also recovers the normal behaviour if $\kappa = \kappa_F$). As is possible to show, this gives the correct (average) energy flows in and out of each sampling region. **When using the method, the number of packets is controlled by continuously adjusting the packet size (energy) in each sampling region. In JEKYLL, this is done once each Λ-iteration based on packet statistics from the previous Λ-iteration. In each sampling region, the SNR is estimated based on the number of packet interactions and compared to some pre-configured target value. The packet size (energy) in the sampling region is then adjusted with the ratio between these, given some pre-configured minimum and maximum values.**

3.4. Matter state solvers

To determine the state of the matter, JEKYLL provides the NLTE solver, as well as the more approximate LTE and **Mazzali & Lucy (1993, hereafter ML93)** solvers. It also provides an option to mix these solvers, e.g. by using the NLTE solver for the ionization and the LTE solver for the excitation, in a manner similar to what is done in ARTIS. In addition, JEKYLL provides a solver to determine the non-thermal electron distribution, used by the NLTE solver.

3.4.1. LTE solver

The LTE solver determines the state of the matter assuming that LTE applies. The populations of ionized **and** excited states are calculated using the Saha ionization and Boltzman excitation equations, respectively. The temperature used may be **that associated with the pure or diluted blackbody radiation field models (T_J or T_R; see Sect. 3.1.1 and K09)**, or the matter temperature determined by some other method **(e.g. thermal equilibrium)**.

3.4.2. ML93 solver

The ML93 solver determines the state of the matter assuming that the radiative rates **dominate**, and is based on the approximations for the populations of ionized and excited states derived by Mazzali & Lucy (1993) and Abbott & Lucy (1985). Following Mazzali & Lucy (1993), the temperature is assumed to be controlled by the radiation field and set to $0.9T_R$, where T_R is the temperature **associated with the diluted blackbody radiation field model (see Sect. 3.1.1 and K09)**.

3.4.3. NLTE solver

The NLTE solver determines the state of the matter by solving the statistical and thermal equilibrium equations for the level populations and the temperature, respectively. The solution is determined in two steps. First, thermal equilibrium is scanned for in a configurable temperature interval (based on the solution from a previous Λ-iteration), solving for statistical equilibrium at each step. Based on this estimate, thermal and statistical equilibrium are simultaneously iterated for until convergence is achieved, using a procedure similar to what is described by L03.

Statistical equilibrium The non-linear statistical equilibrium equation system (Eq. 1) is solved by iteration on the level populations. In each step the system is linearised in terms of changes in the level populations, and the rates and their derivatives are calculated using the previous estimate of these. The linearised system is then solved for the level populations using lower-upper (LU) decomposition and back-substitution. If all number derivatives (explicit and implicit) are included this is equivalent to a Newton-Raphson solver, but we leave this as a configurable choice, and in the simplest configuration only the explicit derivatives (i.e. rates per particle) are included.

The **system of equations** may be solved separately for the states of each atom, ignoring any coupling terms, or for all states at once. As the total number of states may be too large for a coupled solution, we provide the possibility to alternate a decoupled solution with a fully coupled solution for the ionization balance. Typically a decoupled solution works well, but charge-transfer reactions and the source-function radiation field model (see Sect. 3.1.1) may introduce strong coupling terms. Transition rates (Sects. 2.4 and 2.5) for bound-bound and bound-free radiative and collisional processes, as well as for non-thermal, charge-transfer and two-photon processes are all supported, but which ones to include is a configurable choice.

Thermal equilibrium The thermal equilibrium equation (Eq. 2) is solved either using the **bisection** method (initial estimate) or Newton-Raphson's method (refined estimate), in which case an explicit temperature derivative is used. Heating and cooling rates (Sects. 2.4 and 2.5) for bound-bound and bound-free radiative and collisional processes, free-free processes, as well as non-thermal and charge-transfer processes are all supported, but which ones to include is a configurable choice. In addition, an expansion cooling term PdV/dt may also be included, as is motivated in a time-dependent run.

3.4.4. Non-thermal solver

The non-thermal solver determines the non-thermal electron distribution resulting from the radioactive decays, and the fraction of the deposited energy going into heating, excitation and ionization. This is done by solving the Spencer-Fano equation (i.e. the Boltzman equation for electrons) as described in KF92.

3.5. Diffusion solver

The diffusion solver determines the temperature in each cell by solving the thermal energy equation assuming spherical symmetry, homologous expansion, LTE and the diffusion approximation for the radiative flux. This results in a non-linear equation system for the temperature in each cell, which is solved by a Newton-Raphson like technique similar to the one used by Falk & Arnett (1977). Two specific topics require some further discussion though; the Rosseland mean opacity used in the diffusion approximation, and the outer boundary where the diffusion solver is supposed to be coupled to the MC radiative transfer solver.

3.5.1. Opacity

The Rosseland mean opacity used in the diffusion approximation is calculated from the LTE state of the matter and the atomic data. This may sound straightforward, but the bound-bound opacity, and in particular the virtual cell mode (see Sect 3.1.2) complicates things. In the latter case, if the clumps are all optically thin, the opacity may be calculated as a zone average, but otherwise a geometrical aspect enters the problem. Therefore we calculate the Rosseland mean opacity using **a** Monte-Carlo method. In each cell a large number of packets are sampled based on the blackbody flux distribution and the zone filling factors. These packets are then followed until they are absorbed, and their path-length averaged to get the Rosseland mean free path. This gives the Rosseland mean opacity, including the bound-bound contribution as well as the geometrical effects arising in a clumpy **material.**

3.5.2. Outer boundary

If the diffusion solver is coupled to the MC radiative transfer solver at **its** outer boundary **(which is the main purpose of it)**, appropriate boundary conditions must be specified for both solvers. As outer boundary condition for the diffusion solver we use the temperature **in the innermost cell handled by the MC radiative transfer solver**. **As** inner boundary condition for the MC radiative transfer solver we use the luminosity **at this boundary determined with the diffusion solver**. **This is analogous to how the boundary between the diffusion and radiative transfer solvers is treated in Falk & Arnett (1977), except that in JEKYLL these calculations are not coupled and performed separately.** To implement the inner boundary condition for the MC radiative transfer solver we use an approximate method. **During a timestep Δt, packets with total energy $L\Delta t$** are injected at the inner boundary, whereas packets propagating inwards are simply reflected at this boundary. The frequency of the injected packets are sampled from a blackbody distribution at the temperature of the innermost cell.

3.6. Notes on the MC the radiation field

As mentioned in Sect, 3.3.4, the sampling of the MC radiation field is a potential problem with the original method. In our experience this problem is most severe bluewards ∼3000 Å and in the outer region of the ejecta. In principle this could be solved by the method for packet sampling control, but in practice we instead use the source-function approximation (Sect. 3.1.1) bluewards ground-state ionization edges of abundant species (e.g. the Lyman break). The reason for this is twofold. First, to achieve a reasonable SNR in this region might require very large boost factors, which could potentially make the method unstable. Second, in case a residual from two almost cancelling radiative rates (e.g. ionization and recombination in the Lyman continuum) is large enough to be important for the solution, even larger boost factors might be needed to achieve the required SNR. Due to this we use both packet sampling control and the source-function

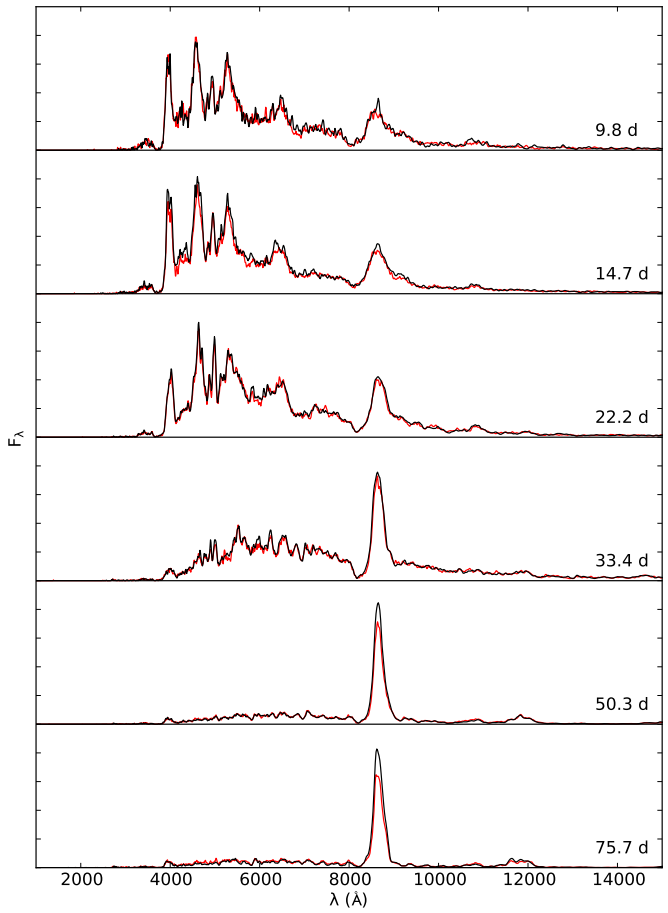

Fig. 1. Comparison of spectral evolution for model 12C as calculated with JEKYLL (black) and ARTIS (red).

approximation in most of the simulations presented here and in Paper 2.

4. Code comparisons

In this section we compare JEKYLL to **ARTIS (K09), SUMO (J11 and J12), and CMFGEN (H98), three** codes which have similar, but not identical capabilities. ARTIS provides a good test of the time-dependent MC radiative transfer, which is very similar, but only supports partial NLTE. SUMO on the other hand, provides a good test of the full NLTE problem, but requires steady-state, so no test of the time-dependent MC radiative transfer is possible. **However, CMFGEN, which is similar to JEKYLL in physical assumptions but different in technique, does provide a test of the full time-dependent NLTE problem. In particular, as it solves the coupled radiation-matter problem and does not rely on Λ-iterations, it provides a way to show that the Lucy method actually converges to the correct solution. Here we present a comparison for a somewhat simplified test case, which still provide a good test of the full time-dependent NLTE problem. The** comparisons to **ARTIS**, **SUMO and CMFGEN** are complementary, and taken together they provide a **thorough** test of the JEKYLL code.

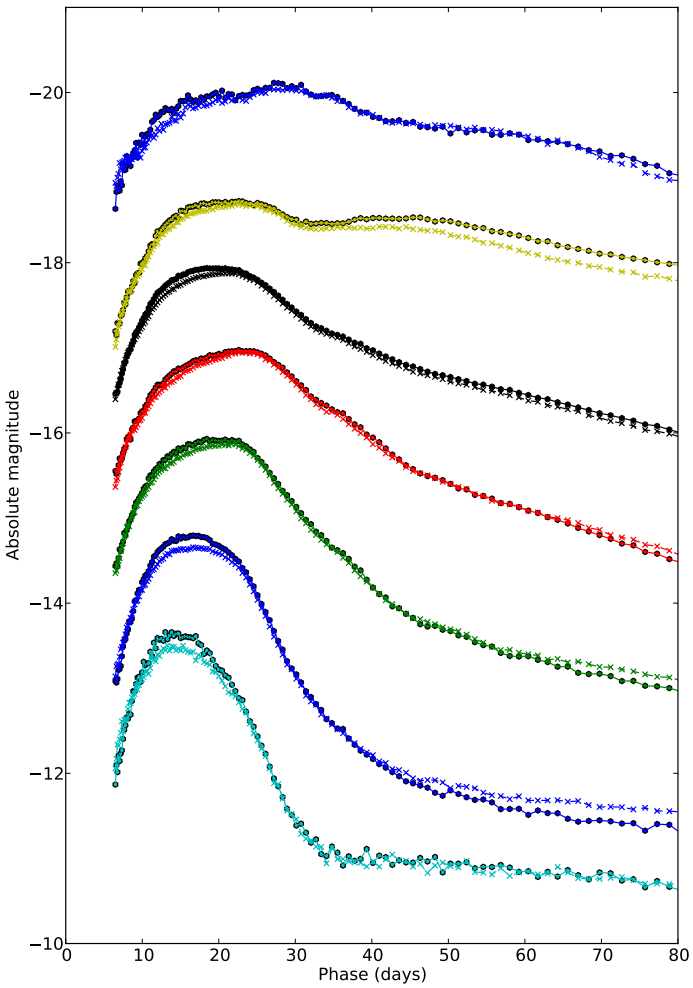

Fig. 2. Comparison of broadband and bolometric lightcurves for model 12C as calculated with JEKYLL (solid lines and circles) and ARTIS (dashed lines and crosses). From bottom to top we show the U **(cyan)**, B (blue), V (green), R (red), bolometric (black), I (yellow) and J (blue) lightcurves, which for clarity have been shifted with 2.0, 2.0, 1.5, 0.5, -1.0, -1.0 and -3.0 mags, respectively

4.1. Comparison with ARTIS

ARTIS is a spectral synthesis code aimed for the photospheric phase presented in K09. Both ARTIS and JEKYLL are based on the **Lucy method**, but ARTIS only supports a simplified NLTE treatment[1] where the excited states are populated according to LTE and the energy deposited by the radioactive decays goes solely into heating. On the other hand, **the current version of** JEKYLL assumes a spherical symmetric geometry, which is not a limitation in ARTIS. In addition, ARTIS calculates the deposition of the radioactive decay energy by Compton scattering, photo-electric absorption and pair production, whereas JEKYLL uses effective grey opacities (based on such calculations). There **are** also differences in the NLTE ionization treatment, in particular with respect to the calculation of photo-ionization rates, and due to this we decided to **run ARTIS** in its LTE mode. This still allows for a complete test of the time-dependent MC radiative transfer, which is the main purpose of the ARTIS comparison.

[1] **A more general NLTE treatment and the inclusion of non-thermal processes in ARTIS are currently under development.**

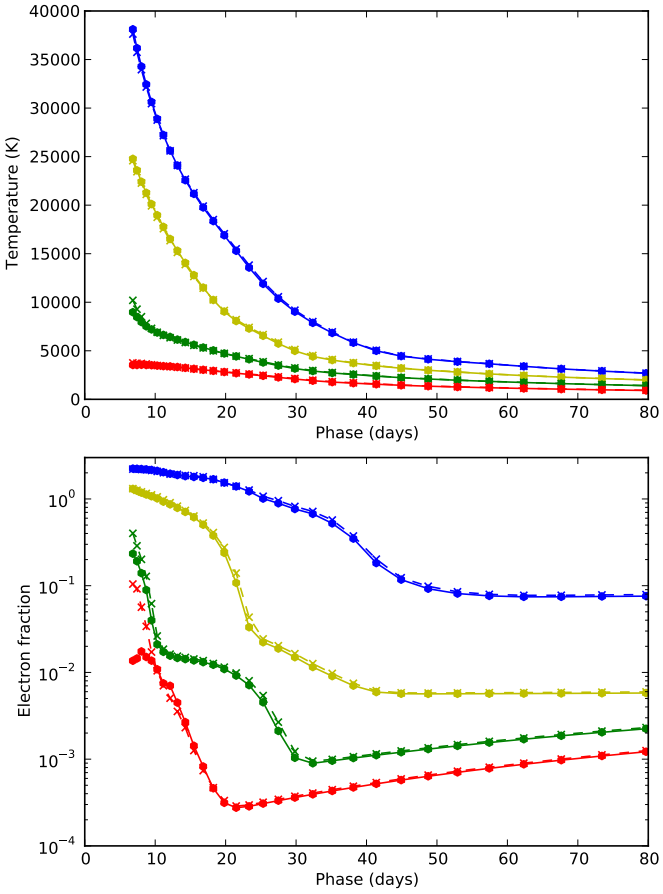

Fig. 3. Comparison of the evolution of the temperature (upper panel) and electron fraction (lower panel) in the oxygen core (blue), inner/outer (yellow/green) helium envelope and the hydrogen envelope (red) for model 12C as calculated with JEKYLL (circles and solid lines) and ARTIS (crosses and dashed lines).

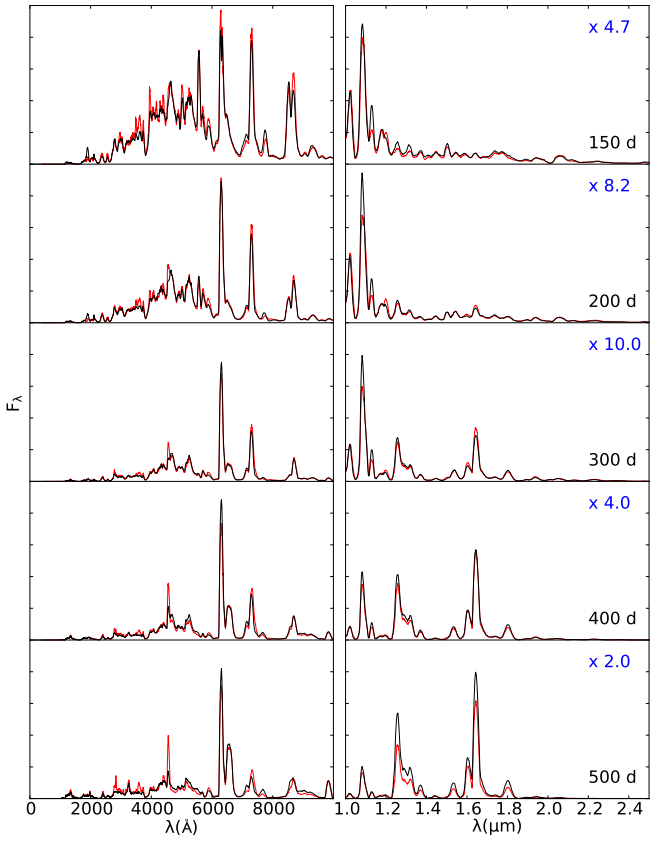

Fig. 4. Comparison of optical (left panel) and NIR (right panel) spectra for model 13G at 150, 200, 300, 400 and 500 days as calculated with JEKYLL (black) and SUMO (red). For clarity the NIR spectra have been scaled with respect to the optical spectra with the factor given in the upper right corner.

For the comparison we use the Type IIb model 12C from J15, which is also used in the application to Type IIb SNe (Sect. 5). **The original model was converted to microscopically mixed form and re-sampled to a finer spatial grid as described in Sect. 5.1.** To synchronize JEKYLL with ARTIS, it was configured to run in time-dependent **(radiative transfer)** mode using the LTE solver, and the ARTIS atomic data was automatically converted to the JEKYLL format. The details of the code configurations and the atomic data used are given in Appendix A, and we find the synchronization good enough for a meaningful comparison. Note that as non-thermal processes are crucial for the population of the excited He I states, the characteristic He I signature of Type IIb SNe is not reproduced.

In Figs. 1 and 2 we compare the spectral evolution and the lightcurves, respectively, whereas in Fig. 3 we compare the evolution of the temperature and the electron fraction. As can be seen, the general agreement is good in both the observed and the state quantities. The most conspicuous discrepancy appears in the Ca II 8498,8542,8662 Å line after ∼40 days, and **gives** rise to a ∼15 percent discrepancy in the *I*-band lightcurve. Another discrepancy appears after ∼50 days in the *B*-band, growing towards ∼15 percent at 80 days. There is also a small (<5 percent) but clear difference in the bolometric tail luminosity, reflecting a similar difference in the radioactive energy deposition. **This is due to the** the more approximate method **for this** used by JEKYLL, which may also explain the differences in the tail broad-band lightcurves. There **are** also minor differences in the diffusion peak lightcurves, most pronounced in the *U*- and *B*-bands, which could be related to the simplified (but different) treatment at high optical depths in ARTIS and JEKYLL (see Appendix A.1). Summarizing, although there are some minor differences in the spectra and the lightcurves, we find the overall agreement to be good.

4.2. Comparison with SUMO

SUMO is a spectral synthesis code aimed for the nebular phase presented in **J11 and J12**. Similar to JEKYLL, it uses a Λ-iteration scheme, where the radiative transfer is solved with a MC method and the state of the matter determined from statistical and thermal equilibrium. Except for the **(radiative transfer)** steady-state assumption, which is required by SUMO and an option in JEKYLL, the main difference between SUMO and JEKYLL is the MC technique used. Whereas JEKYLL is based on the **Lucy method**, where conservation of packet energy is enforced, SUMO uses another approach. Except for electron scattering and excitations to high lying states, the packet energy absorbed in free-free, bound-free and bound-bound processes is not re-emitted. As long as these processes are included in the emissivity from which the packets are sampled, this gives the correct solution in the limit of convergence. However, it could be **an issue** for the rate of convergence, in particular at high ab-

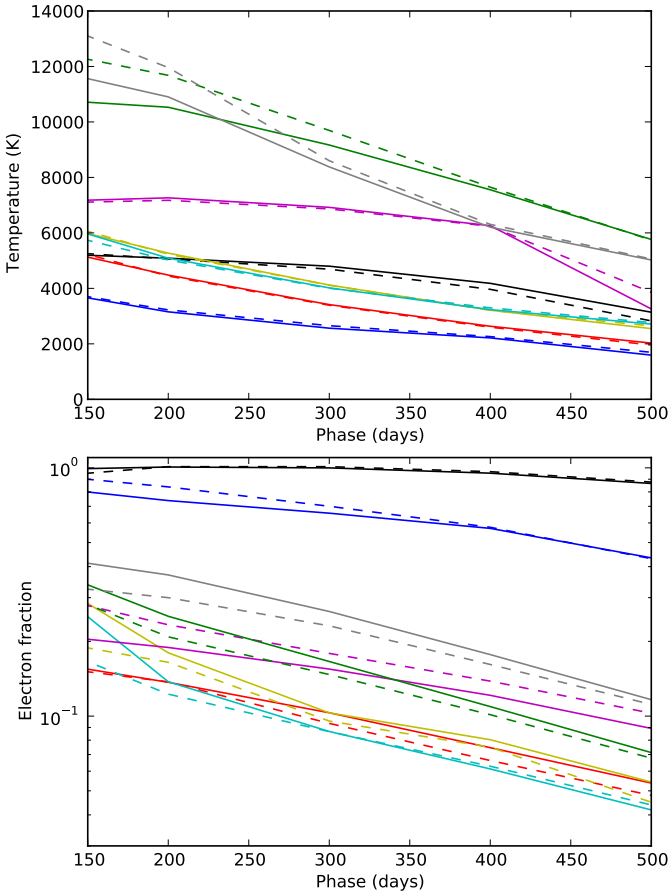

Fig. 5. Comparison of the evolution of the temperature (upper panel) and the electron fraction (lower panel) for model 13G in the **Fe/Co/He (black),** Si/S (blue), O/Si/S (red), O/Ne/Mg (yellow), O/C (cyan), He/C (magenta), He/N (green) and H (grey) zones as calculated with JEKYLL (solid lines) and SUMO (dashed lines).

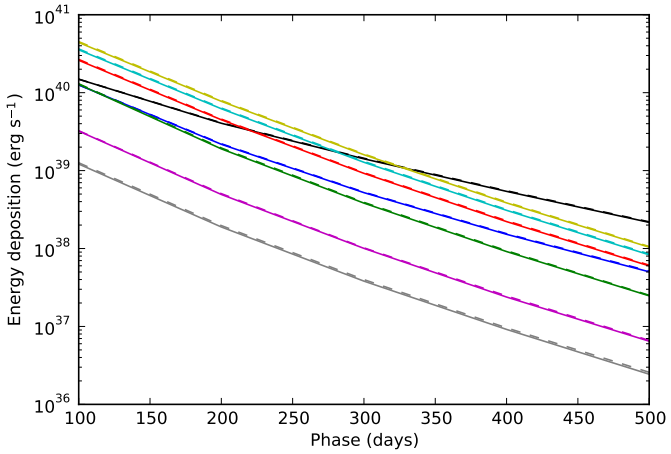

Fig. 6. Comparison of the evolution of the radioactive energy deposition for model 13G in the Fe/Co/He (black), Si/S (blue), O/Si/S (red), O/Ne/Mg (yellow), O/C (cyan), He/C (magenta), He/N (green) and H (grey) zones as calculated with JEKYLL (solid lines) and SUMO (dashed lines).

sorption depths, and the method is probably not suited for the photospheric phase. There are also a few differences in the physical assumptions. Whereas JEKYLL correctly samples the frequency dependence of the bound-free emissivity, this is done in a simplified manner for all species but hydrogen by SUMO. On the other hand, JEKYLL does not take the escape probability from continua and other lines in the Sobolev resonance region into account. However, in general the physical assumptions are similar.

For the comparison we use the Type IIb model 13G from J15, and run models with JEKYLL at 150, 200, 300, 400 and 500 days. To synchronize **JEKYLL** with SUMO, it was configured to run in steady-state mode using the NLTE solver, and we have tried to synchronize the atomic data as much as possible. The details of the code configurations and the atomic data used are given in Appendix A, and although not complete, we find the synchronization good enough for a meaningful comparison.

A comparison of the spectral evolution is shown in Fig. 4, and in Figs. 5 **and 6** we compare the evolution of the temperature, the electron fraction **and the radioactive energy deposition** in each of the different nuclear burning zones (see J15). As can be seen, the general agreement of the spectra is quite good, although the match is slightly worse at 500 days. The largest discrepancies are seen in the Mg I] 4571 Å line, the O I 11290,11300 Å line before 300 days, the He I 10830 Å line at 200-300 days, and a number of features originating from the Fe/Co/He zone at 500 days. That one of the largest discrepancies is seen in the Mg I] 4571 Å line is not surprising as magnesium is mainly ionized and the Mg I fraction is small (see J15). This makes the strength of the Mg I] 4571 Å line sensitive to this fraction, in turn sensitive to the network of charge transfer reactions.

The evolution of the temperature shows a good agreement and the differences are mainly below ∼5 percent. An exception is the He/N and H zones at early times, and in particular at 150 days where the difference is ∼15 percent. The evolution of the electron fraction shows a worse agreement, but the differences are mainly below ∼10 percent. Again, the agreement is worst at early times, and in particular at 150 days when the electron fractions in the O/Ne/Mg and O/C zones differ by ∼30 percent. This discrepancy is reflected in e.g. the O I 11290,11300 Å line discussed above, but in general the spectral agreement at 150 days is quite good.

The evolution of the radioactive energy deposition shows an excellent agreement. This shows that the radiative transfer of the g-packets (Sect. 3.3.1 and 3.3.2), representing the γ-rays (and leptons) emitted in the radioactive decays, as well as the virtual cell method (Sect. 3.1.2 and 3.3.2), used to represent the macroscopic mixing of the material, works as intended. Summarizing, although there are some notable differences both in the spectra and the state variables, we find the overall agreement to be good, in particular as the data and the methods are not entirely synchronized.

4.3. *Comparison with CMFGEN*

CMFGEN is a general purpose spectral synthesis code presented in its steady-state version in H98, and extended with time-dependence in Dessart & Hillier (2008, 2010) and Hillier & Dessart (2012) and non-thermal processes in Dessart et al. (2012). It is similar to JEKYLL in the physical assumptions, but use a different method to solve the NLTE problem, where the coupled system of differential equations for the matter and the radiation field is solved by a linearization technique. The potential difficulties with convergence in Λ-iteration based methods (Sect. 2.1) are therefore avoided, and the comparison provides a good test of the convergence

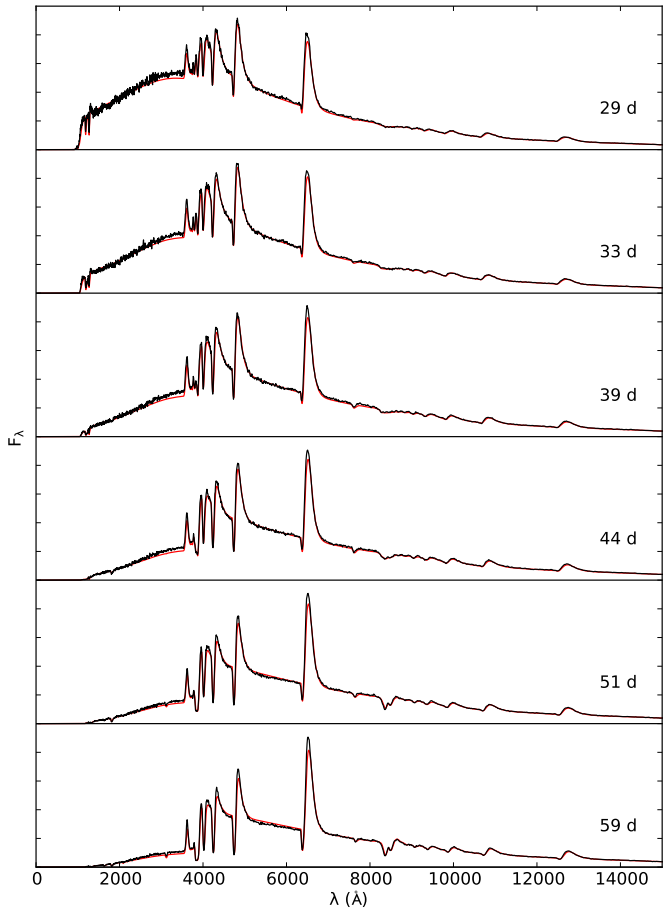

Fig. 7. Comparison of spectral evolution for the test model as calculated with JEKYLL (black) and CMFGEN (red).

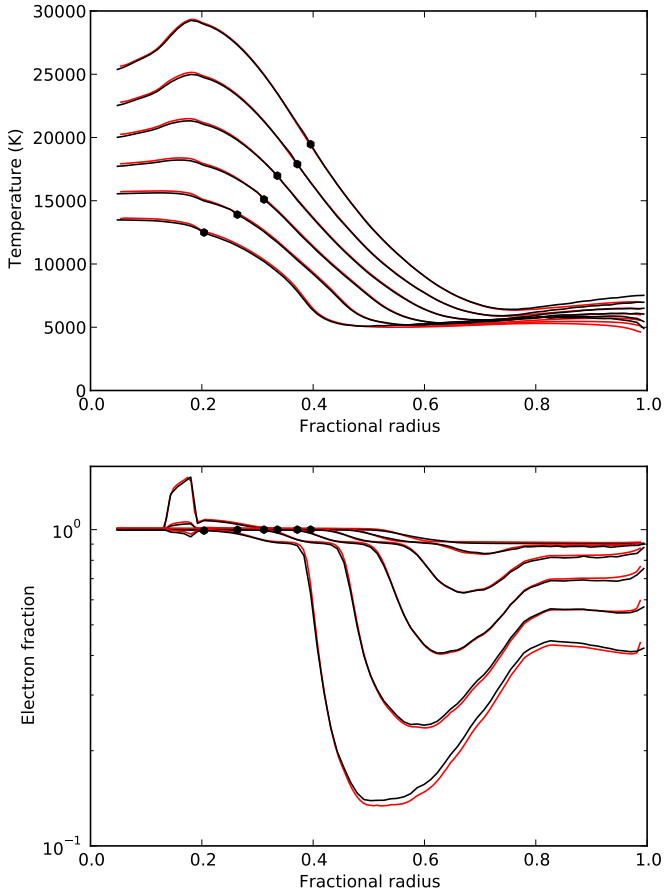

Fig. 8. Comparison of the evolution of the temperature (upper panel) and electron fraction (lower panel) at the same epochs as in Fig. 7 for the test model as calculated with JEKYLL (black) and CMFGEN (red). The border between the diffusion solver and the MC radiative transfer solver have been marked with black circles.

properties of the Λ-iteration and MC based method used in JEKYLL (i.e. the one by Lucy). The main difference in the physical assumptions is that JEKYLL assumes steady state for the matter, whereas CMFGEN does not. In addition, CMFGEN does not rely on the Sobolev approximation, but this is likely of less importance at the high velocity gradients present in SN ejecta.

For the comparison we use a model of a red supergiant of 15 $M_\odot$ initial mass, evolved with MESA (Paxton et al. 2011, 2013) and exploded with an energy of 1 Bethe with the hydrodynamical code HYDE (E14). The JEKYLL and CMFGEN simulations begin at 25 days, and for the test we use a simplified composition consisting of hydrogen, helium, oxygen and calcium. As it turned out to be difficult to switch off the time-dependence in CMFGEN in a self-consistent way, we instead added an option in JEKYLL to use the time-dependent NLTE rate equations. This is achieved by adding the time-derivative

$$\rho \frac{D(n_{I,j}/\rho)}{Dt} \tag{4}$$

to the right-hand side of Eq. 1 (see Dessart & Hillier 2008). This accounts for the effect of time-dependence on the degree of ionization, which is the most important one, at least in the test model. Note that time-dependence is only added in this limited form to facilitate the comparison with CMFGEN, and is not explored further in the paper. A general upgrade of JEKYLL to full time-dependence will be presented in a forth-coming paper.

A comparison of the spectral evolution is shown in Fig. 7 and in Fig. 8 we compare the evolution of the temperature and the electron fraction. As can be seen, the overall agreement is good in both the spectra and the matter quantities. The largest differences in the spectra are a somewhat higher flux in the Balmer continuum and a bit stronger emission in the Balmer lines in the JEKYLL model. The electron fraction is in good agreement, but the temperature is slightly higher in the outer region in the JEKYLL model. Given that time-dependence is only partly implemented in JEKYLL, and is missing in the thermal energy equation, differences at this level is not surprising. The good overall agreement found in both the spectra and the matter quantities shows that the Λ-iteration and MC based method used in JEKYLL (i.e. the one by Lucy) does indeed converge to the correct solution. Departures from LTE are large (typically a factor of ten or larger) in the optically thin region, so although based on a simplified model, the comparison provides a good test of the time-dependent NLTE capabilities.

5. Application and tests

In this section we provide an example of a time-dependent NLTE model based on a fully realistic ejecta model. The ejecta model (12C) is taken from the set of Type IIb models constructed by J15, and among those it was found to give the best match to the observed nebular spectra (J15) and lightcurves (E15) of SN 2011dh. For a deeper discussion of the model and a comparison to SN 2011dh we refer to Paper 2, where we also explore other models.

In addition to a brief discussion of the example model and its evolution, we investigate the effect of NLTE on the spectra and the lightcurves, in particular with respect to non-thermal ionization and excitation. Based on the example model, we also investigate the convergence of the Λ-iterations, and provide tests of the most important extensions to the original Lucy method, i.e. the use of a diffusion solver in the inner region, the packet sampling control and the Markov-chain solution to the MC state-machine.

5.1. *Ejecta model*

A full description of the Type IIb model 12C is given in J15, but we repeat the basic properties here. It is based on a model by Woosley & Heger (2007) with an initial mass of 12 $M_\odot$, from which we take the masses and abundances for the carbon-oxygen core and the helium envelope. We assume the carbon-oxygen core to be fully mixed and to have a constant **(average)** density, and the helium envelope to have the same density profile as the best-fit model for SN 2011dh by Bersten et al. (2012). In addition, a 0.1 $M_\odot$ hydrogen envelope based on models by Woosley et al. (1994) is attached. **Note that the ejecta model explored here is a microscopically mixed version, in which the abundances in the nuclear burning zones (see J15) have been averaged. For the macroscopically mixed version we refer to Paper 2, where we also discuss the effect of this difference on the model evolution. To be suitable for modelling in the photospheric phase, the original ejecta model has also been resampled to a finer spatial grid.**

5.2. *Model evolution*

JEKYLL was configured to run in time-dependent (radiative transfer) mode using the NLTE solver based on an updated version of the J15 atomic data, and we give the details of the configuration and the atomic data in Appendix A. The model was evolved from 1 to **100** days, and the initial temperature profile was taken from the best-fit model for SN 2011dh from E15. **Figure 10 shows the spectral evolution, whereas Fig. 11 shows the lightcurves and Fig. 9 the evolution of the temperature and the electron fraction. In Fig. 10 we also display the process giving rise to the emission, based on the last emission events for the MC packets (excluding electron scattering).**

The main signature of a Type IIb SN is the transition from a hydrogen to a helium dominated spectrum, and this is well reproduced by the model. Initially, the hydrogen lines are strong and emission from the hydrogen envelope is dominating. Between 10 and 15 days the helium lines appear, grow stronger, and eventually dominate the spectrum at ∼40 days. Hydrogen line emission disappears on a similar time-scale, completing the transition, although the Balmer lines remain considerably longer in absorption. **After ∼40 days the carbon-oxygen core gets increasingly transparent and the amount of realism in the microscopically mixed model starts to degrade, exemplified by the strong calcium NIR triplet at 100 days. As is demonstrated in Paper 2, the macroscopically mixed version of the model does a considerable better job in reproducing observations in this phase. The lightcurves show the characteristic bell shape of stripped-envelope (SE; Type IIb, Ib and Ic) SNe, and as discussed in Paper 2 their change in shape with effective wavelength (as e.g. a broader peak for redder bands) is in good agreement with observational studies. It is worth noting that the behaviour of model 12C is similar to that of the NLTE models of SE SNe presented by Dessart et al. (2015, 2016). Those models were evolved with CMFGEN and in particular the Type IIb model 3p65Ax1 shares many properties with model 12C.**

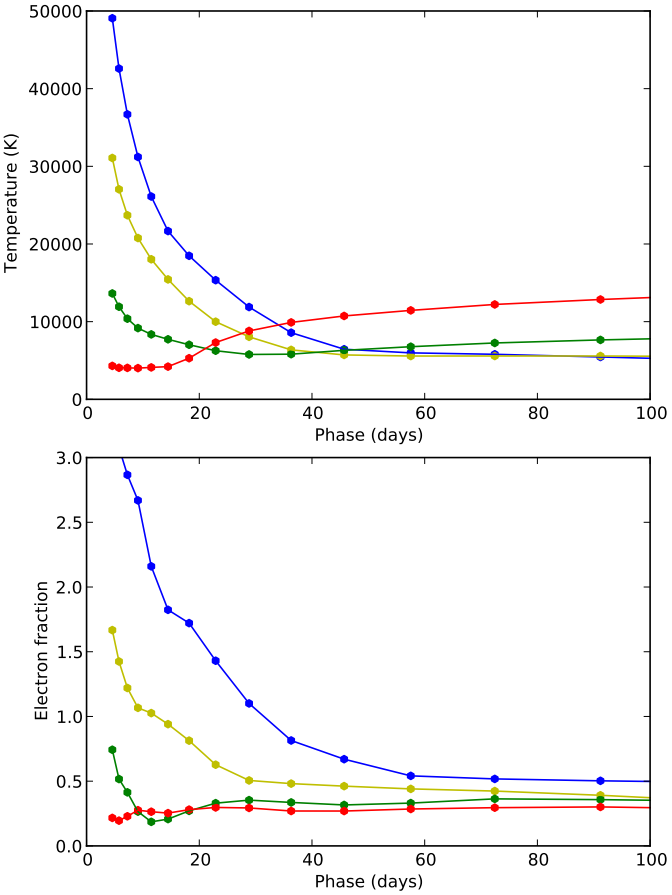

Fig. 9. Evolution of the temperature (upper panel) and electron fraction (lower panel) in the oxygen core (blue), inner/outer (yellow/green) helium envelope and the hydrogen envelope (red) for model 12C.

5.3. *The effect of NLTE*

Figures 12 and 13 show the bolometric lightcurve and the spectral evolution of model 12C calculated with JEKYLL with and without non-thermal ionization and excitation. Before 10 days both the bolometric lightcurve and the spectral evolution are very similar, after which they start to differ in several aspects. This turning point coincides with the time when the radioactive energy deposition becomes important outside the photosphere (**see Paper 2**). The most striking difference in the spectral evolution is the absence of (strong) helium lines in the model without non-thermal processes. **This well-known effect was pointed out already by Lucy (1991) and was later confirmed using CM-**

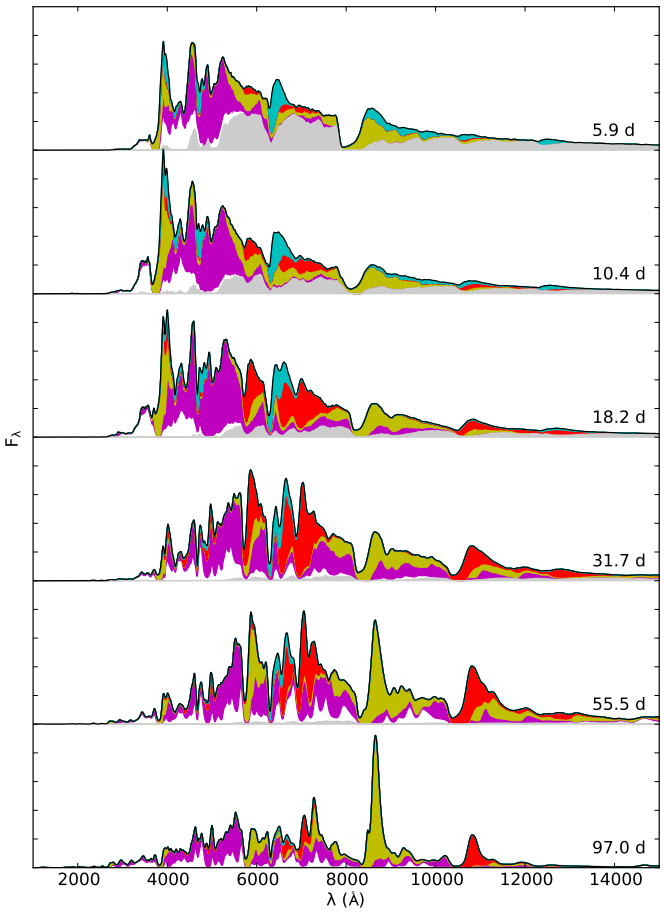

Fig. 10. Spectral evolution in the optical (left panel) and NIR (right panel) for model 12C as calculated with JEKYLL. In the spectra we show the contributions to the emission from bound-bound transitions of hydrogen (cyan), helium (red), carbon-calcium (yellow), scandium-manganese (white) and iron-nickel (magenta) as well as continuum processes (grey).

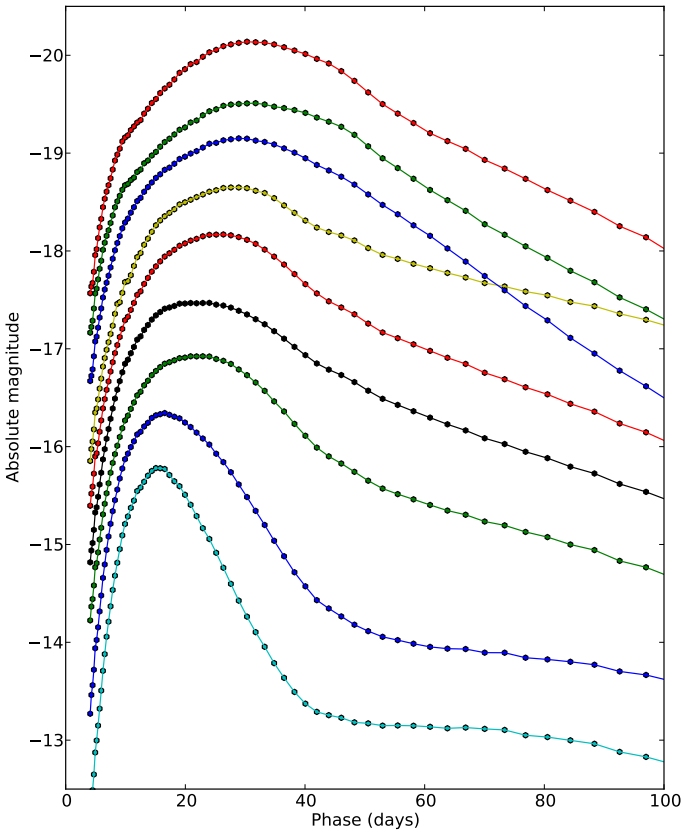

Fig. 11. Broadband and bolometric lightcurves for model 12C as calculated with JEKYLL . From bottom to top we show the U (cyan), B (blue), V (green), R (red), bolometric (black), I (yellow), J (blue), H (green) and K (red) lightcurves, which for clarity have been shifted with 2.6, 1.2, 0.0, -1.4, -3.5, -4.4, -5.8, -7.5, -8.9 mags, respectively.

FGEN by Dessart et al. (2012). Non-thermal excitation and ionization are essential to populate the excited levels of He I, which is in turn required to produce the lines observed. As discussed by Lucy (1991), the population process is subtle, as ionization of He I is amplified by photo-ionization from the excited levels, which proceeds at a rate far exceeding the non-thermal one.

Less known is the quite strong effect on the bolometric lightcurve, where the diffusion peak of the model with non-thermal processes is considerably broader. The reason for this is the increased degree of ionization, and therefore the increased electron scattering opacity. This is illustrated by Fig. 14, which shows the evolution of the electron fraction in the carbon-oxygen core and the helium and hydrogen envelopes. In the model with non-thermal processes, the electron fraction in the helium envelope drops much slower than in the model without. Due to the lower ionization potential, the effect is much less pronounced in the carbon-oxygen core and the hydrogen envelope. In **Fig. 12** we also show **the bolometric lightcurve for the LTE version of model 12C used for the comparison with ARTIS in Sect. 4.1**. This model shows an even narrower bolometric lightcurve, which is related to the even lower degree of ionization in this model. **Note that the atomic data used for this model differs a bit from that used for the NLTE models in this section, but this difference does not significantly affect the bolometric lightcurve**.

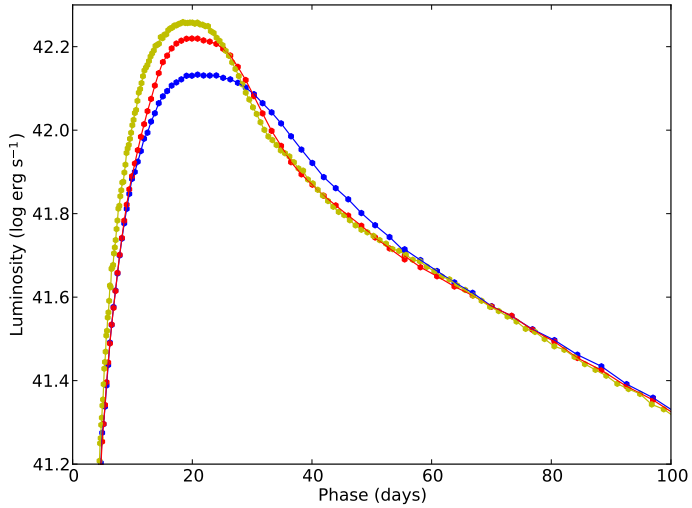

Fig. 12. Bolometric lightcurve for model 12C calculated with (blue) and without (red) non-thermal ionization and excitation. We also show the bolometric lightcurve for the LTE version of model 12C (yellow) presented in Sect. 4.1.

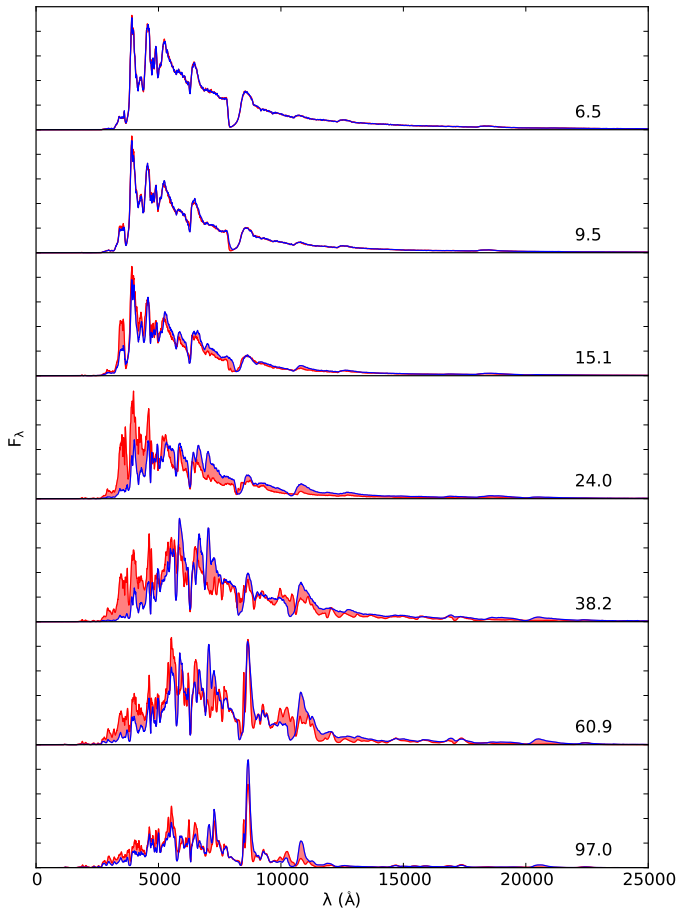

Fig. 13. Spectral evolution for model 12C calculated with (blue) and without (red) non-thermal ionization and excitation, **where the difference has been highlighted in shaded red**.

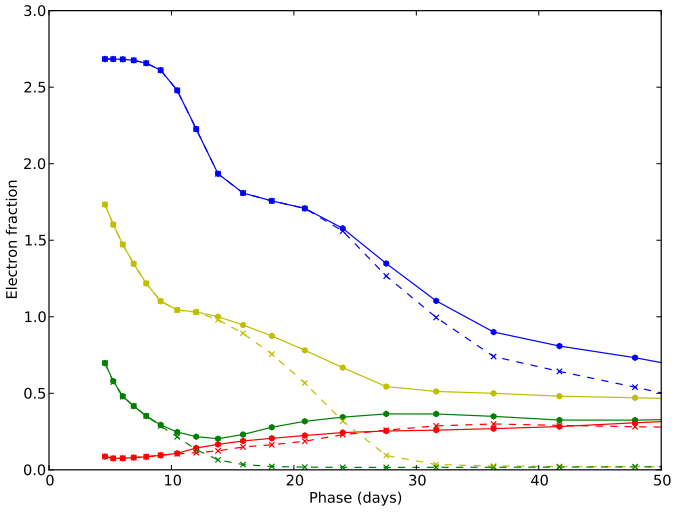

Fig. 14. Evolution of the electron fraction in the oxygen core (blue), inner/outer (yellow/green) helium envelope and the hydrogen envelope (red) for model 12C calculated with (circles and solid lines) and without (crosses and dashed lines) non-thermal ionization and excitation.

5.4. Convergence of the Λ-iterations

As mentioned in Sect. 3, JEKYLL use a fixed (but configurable) number of Λ-iterations. In time-dependent **(radiative transfer)** mode, this is the number of Λ-iterations per time-step, and corresponds to some (unknown) number of effective Λ-iterations depending on the length of the time-step and the rate at which the state is changing. The time-dependent NLTE **run in this section uses** a logarithmic time-step of 5 percent and 4 Λ-iterations per time-step. In Figs. 15 and 16 we show the lightcurves and the temperature and electron fraction, respectively, for three such runs using 2, 4 and 8 Λ-iterations per time-step. Note, that to speed up the calculations we used coarser spatial sampling, slightly simplified atomic data and fewer packets than in the original model. As can be seen, convergence is fast, and more than 4 iterations per time-step does not make a significant difference. Even the 2-iterations run is good enough for most purposes, although there is a ∼25 percent difference in the *U*-band during the drop from the peak onto the tail. The comparisons to ARTIS in Sect. 4.1 **behave** in a similar way, but the shorter time-step of 1 percent, and possibly a faster convergence in the LTE case, **make** even a single iteration run well converged, showing less discrepancy than the 2-iterations run in Figure 15. **The comparisons to CMFGEN in Sect. 4.3 also behave similarly. Using more than 4 Λ-iterations per time-step does not make a significant difference, and using four instead of 2 Λ-iterations only marginally changes the spectra. As discussed in Sect. 4.3, in this case we also know that the Λ-iteration is converging to the correct solution (i.e. the one calculated with CMFGEN). Together with the nice convergence properties for model 12C, this is assuring, although further comparisons to CMFGEN would be interesting.**

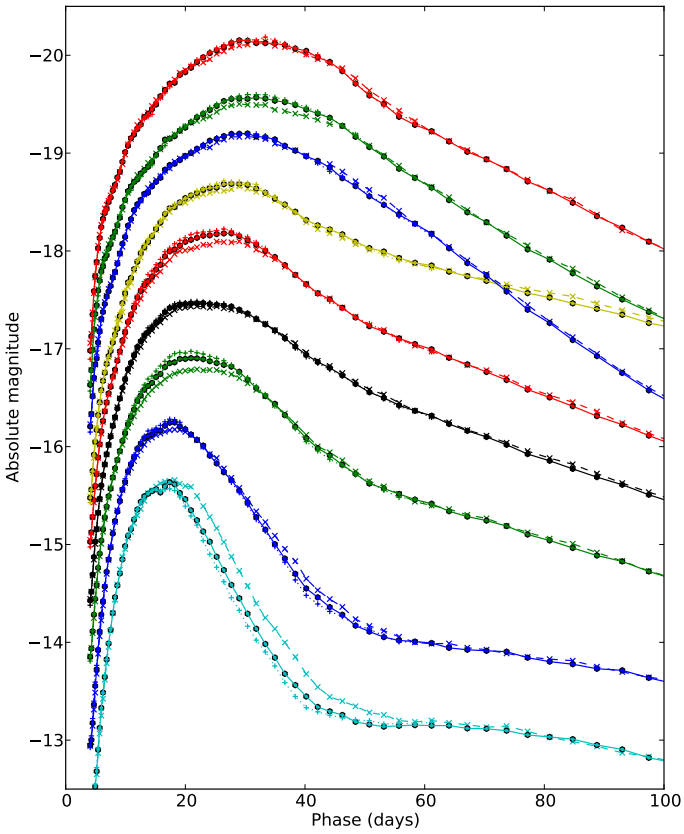

Fig. 15. Broad-band and bolometric lightcurve for model 12C as calculated with JEKYLL using 2 (dashed lines and crosses), 4 (solid lines and circles) and 8 (dotted lines and pluses) Λ-iterations per time-step. Otherwise as described in Fig. 11.

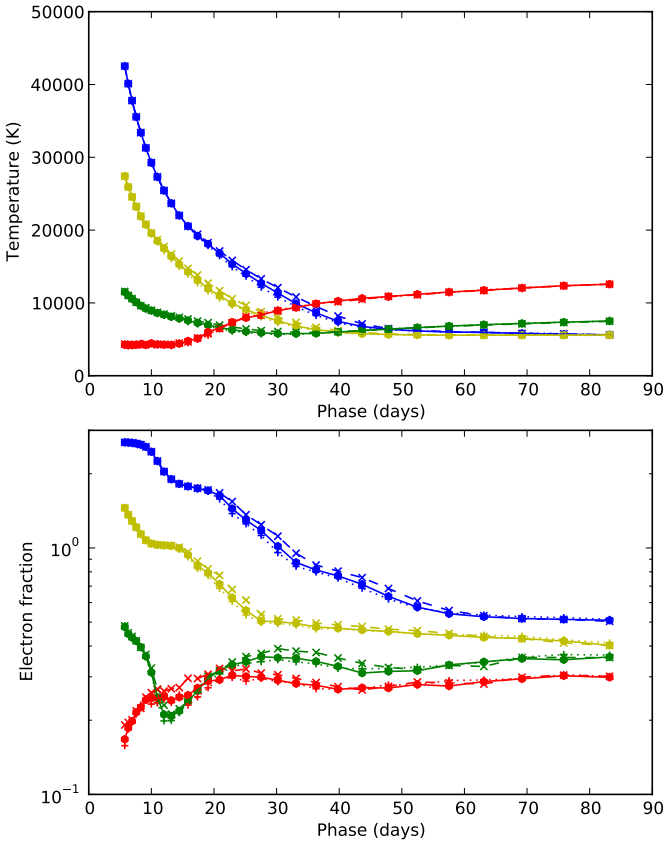

Fig. 16. Temperature (upper panel) and electron fraction (lower panel) for model 12C as calculated with JEKYLL using 2 (dashed lines and crosses), 4 (solid lines and circles) and 8 (dotted lines and pluses) Λ-iterations per time-step. Otherwise as described in Fig. 9.

5.5. Test of extensions

5.5.1. The use of a diffusion solver

The use of the diffusion solver in the inner region speed up calculations in the early phase, and it is used it in all simulations except the comparison with SUMO. It is therefore of interest to investigate how the use of it and the depth at which it is coupled influence the solution. To achieve this, we have run model 12C with the diffusion solver coupled at an optical depth of 50, 100 and 200 using the same simplified set-up as described in Sect. 5.4. At these coupling depths, the diffusion solver is only used until 21, 15 and 12 days, respectively, so in the last case most of the diffusion peak is actually calculated using the MC radiative transfer solver alone. The results show no significant differences in the spectra and only small differences in the matter quantities, which justifies the use of the diffusion solver, at least at an optical depth of 50 or more. It is also interesting to return to the comparison with CMFGEN and look at Fig. 8, where we have marked the border between the diffusion solver and the MC radiative transfer solver. As we can here compare to the correct solution (i.e. the one provided by CMFGEN), it is evident that the use of a coupled diffusion and MC radiative transfer solver works well.

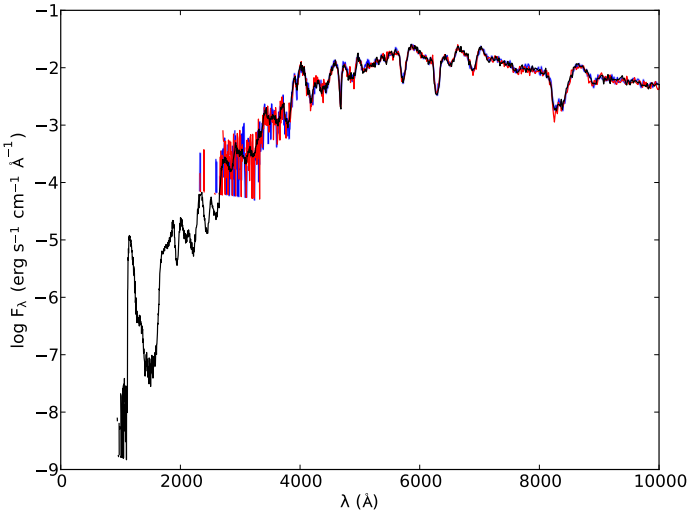

Fig. 17. Spectra for model 12C at 36.3 days with (black) and without (red) packet control activated, as well as with (red) and without (blue) the Markov-Chain solution activated.

5.5.2. The packet sampling control

The method for packet sampling control was introduced in Sect. 3.3.4, and is used to decrease the noise in the radiation field estimators. As a test of it, we have re-run the MC radiative transfer for model 12C with and without packet sampling control activated. In doing this we have loaded the matter state from the original model 12C run and kept it fixed (i.e. we have not run any Λ-iterations to improve it). Fig. 17 shows the spectrum for model 12C at 36.3 days with (black) and without (red) packet sampling control activated. The packet sampling control was configured to maintain a SNR of 3 percent between the Lyman break and 25000 Å with a minimum boost factor of 1 and and a maximum boost factor of 10^5. As seen in Fig. 17, the two spectra agree well as long as the SNR is good in both, which shows that the method reproduces the correct radiation field. In addition, in the region redwards ∼3000 Å, a SNR of ∼3 percent is maintained (almost) all the way to the Lyman break in the model with packet sampling control, but in the model without there is no MC packets at all below ∼2500 Å. The average boost of the number of packets is ∼4, whereas the bost factors in the blue region approach the maximum value allowed (10^5). Without packet sampling control the same SNR in the blue region could only have been achieved by increasing the number of packets by this huge factor.

5.5.3. The Markov-Chain solution

The Markov-Chain solution to the Lucy state-machine was introduced in Sect. 3.3.4 as a way to sample the emission frequency more efficiently. As a test of it, we have re-run the MC radiative transfer for model 12C with and without the Markov-Chain solution activated. As in Sect. 5.5.2, we have loaded the matter state from the original model 12C run and kept it fixed. Fig. 17 shows the spectrum for model 12C at 36.3 days with (red) and without (blue) the Markov-Chain solution activated. As seen in Fig. 17, the spectra agree well, which shows that the Markov-Chain solution produces the same radiation field as the original

state-machine. The speed-up of the MC radiative transfer when using the Markov-Chain solution is ∼50 at 1 day, increases to ∼150 at 4 days and then declines and levels out at ∼10, so clearly this method is essential at early times, and otherwise most helpful in reducing the computational effort.

6. Conclusions

We present and describe JEKYLL, a new code for modelling of SN spectra and lightcurves. The code assumes homologous expansion, spherical symmetry and steady state for the matter, but is otherwise capable of solving for the time-evolution of the matter and the radiation field in full NLTE. **The method used is an extension of the MC based Lucy method, here tested for the first time in its time-dependent NLTE version.** In particular, it includes a detailed treatment of non-thermal excitation and ionization, **as well as a method to account for the macroscopic mixing that occurs in the explosion. We also describe how to speed up the calculation by using a diffusion solver in the inner region, and by using Markov-chains to sample the packet frequency more efficiently In addition, we introduce a novel method to control the sampling of the radiation field, which is used to reduce the noise in the radiation field estimators.**

We also present comparisons with the **ARTIS, SUMO and CMFGEN codes. The ARTIS and SUMO codes** are similar to JEKYLL in some, but not all, aspects, **and the comparisons provide tests of the time-dependent MC radiative transfer and the steady-state NLTE capabilities, respectively. The CMFGEN code is similar in terms of physics, but uses a different method, where the coupled system of differential equations for the matter and the radiation field is solved by a linearization technique. This comparison, which is done with a somewhat simplified ejecta model, provides a test of the time-dependent NLTE capabilities of JEKYLL. All comparisons** show a good agreement in the observed quantities, as well as the state variables, **and together they provide a thorough test of the JEKYLL code. In particular, the comparison with CMFGEN shows that the MC based Lucy method, where the time-dependent NLTE problem is solved through Λ-iterations, does indeed converge to the correct solution. This has previously only been shown for the steady-state NLTE case in a pure hydrogen SN atmosphere (L03).**

Finally, we present an example of the time-dependent NLTE capabilities of JEKYLL using a realistic ejecta model for a Type IIb SN. This model belongs to the set of Type IIb models by J15, which are explored in more detail and compared to observations in Paper 2. Based on the example model we investigate the effect of NLTE, and find strong effects even on the bolometric lightcurve. This casts some doubts on LTE-based modelling of the bolometric lightcurve commonly used in the literature. For example non-thermal ionization turns out to have a strong effect on the ionization level in the helium envelope, which introduce a coupling between the mixing of the radioactive ^{56}Ni and the diffusion time not accounted for in LTE-based models. **We also use the example model to test some of the important extension of the Lucy method. Among others, these tests show that the Markov-chain solution to the MC state-machine may speed-up the calculations in the early phase with large factors, and that the method for packet sampling control may improve the SNR in noisy wavelength regions with large factors at a modest computational cost.**

7. Acknowledgements

We thank Kristoffer Spricer for introducing us to Markov-chains, and for the suggestion to use a Markov-chain model for the Lucy method state-machine.

Appendix A: Configuration and atomic data

Appendix A.1: Comparison to ARTIS

To synchronize JEKYLL with ARTIS, both codes were configured to use a LTE solution for the matter based on T_J, **the temperature associated with the pure blackbody radiation field model (see Sect. 3.1.1 and K09), and the MC radiative transfer solver used by JEKYLL was configured to include radiative and collisional bound-bound and bound-free processes as well as free-free processes.** In addition, ARTIS was configured to use its grey approximation (see K09) before ∼6 days and below an optical depth of 100, and JEKYLL was configured to use the diffusion solver below an optical depth of 50.

The atomic data used by ARTIS is described in K09, but was restricted to the first four ionization stages, using the fourth as closure. As all of the atomic data is stored in data-files in a well-defined format, it was quite straight-forward to automatically convert it to the JEKYLL atomic data format, and it should be fully synchronized. ARTIS and JEKYLL were both configured to use a logarithmic time-step of 1 percent and single Λ-iteration per time-step, which is the standard procedure in ARTIS. As discussed in **Sect 5.4**, due to the short time-step, these runs are still well converged.

Appendix A.2: Comparison to SUMO

As much as possible, we have synchronized the configuration and the atomic data used by JEKYLL with that used for the modelling in J15. To achieve this, JEKYLL was configured to run in steady-state mode, and to use a full NLTE solution including the following; radiative bound-bound, bound-free and free-free processes, collisional bound-bound processes, non-thermal excitation, ionization and heating, as well as charge-transfer and two-photon processes. JEKYLL was also configured to use a recombination correction in a manner similar to SUMO (see J11), in which case detailed balance was not enforced.

The atomic data used for the modelling in J15 is described in J11 and Jerkstrand et al. (2012). In the case it was stored in data-files in a well-defined format, as for e.g. energy levels and spontaneous emission rates, it was automatically converted to the JEKYLL atomic data format, and otherwise it was added manually to the JEKYLL atomic data files based on the descriptions in J11 and Jerkstrand et al. (2012). Although not complete, the synchronization of the atomic data and the methods should be good enough for a meaningful comparison.

Appendix A.3: Comparison to CMFGEN

To syncronize JEKYLL with CMFGEN, JEKYLL was configured run in time-dependent (radiative transfer) mode, and to use a full NLTE solution including the following; radiative bound-bound, bound-free and free-free processes, as well as collisional bound-bound and bound-free processes. JEKYLL was also configured to use the time-dependent NLTE rate equations and to use the diffusion solver below an optical depth of 100. In addition, to assure good sampling of the radiation field, packet control (see Sect. 3.3.4) was turned on and the source-function

approximation (see Sect. 3.1.1) was used bluewards the Lyman break.

The atomic data for the simplified composition of hydrogen, helium, oxygen and calcium were automatically converted from the well-defined format of CMFGEN to that of JEKYLL, and should therefore be fully synchronized. CMFGEN and JEKYLL were both configured to use a logarithmic time-step of 2.5 percent, and JEKYLL was configured to use 4 Λ-iterations per time-step. As discussed in Sect. 5.4, this gives a well converged solution.

Appendix A.4: ***Application***

JEKYLL was configured to run in time-dependent **(radiative transfer)** mode, and to use a full NLTE solution including the following; radiative bound-bound, bound-free and free-free processes, collisional bound-bound and bound-free processes, non-thermal excitation, ionization and heating, as well as two-photon processes. JEKYLL was also configured to use the diffusion solver below an optical depth of 50, and a recombination correction while still enforcing detailed balance. In addition, to assure good sampling of the radiation field, packet control (see Sect. 3.3.4) was turned on and the source-function approximation (see Sect. 3.1.1) was used bluewards the Lyman break. The logarithmic time-step was set to 5 percent and the number of Λ-iterations per time-step was set to 4. As discussed in Sect. 5.4, this gives a well converged solution.

The atomic data used is the same as for the comparison with SUMO (Sect. A.2), but with the following modifications. The highest ionization stage was increased to VI for all species, and the stage III ions were updated to include at least 50 levels for elements lighter than Sc, and at least 200 levels for heavier elements, using online data provided by NIST[2] and R. Kurucz[3]. Total recombination rates for the stage III ions were adopted from the online table provided by S. Nahar[4] whenever available, and otherwise from Shull & van Steenberg (1982). For ionization stages IV to VI we only included the ground-state multiplets, adopted the photo-ionization cross-section by Verner & Yakovlev (1995) and Verner et al. (1996) and assumed the populations to be in LTE with respect to stage IV.

Appendix A.5: Splitting the MC state-machine

TBD

References

Abbott, D. C. & Lucy, L. B. 1985, ApJ, 288, 679
Bersten, M. C., Benvenuto, O. G., Nomoto, K., et al. 2012, ApJ, 757, 31
Cannon, C. J. 1973a, J. Quant. Spec. Radiat. Transf., 13, 627
Cannon, C. J. 1973b, ApJ, 185, 621
Dessart, L. & Hillier, D. J. 2008, MNRAS, 383, 57
Dessart, L. & Hillier, D. J. 2010, MNRAS, 405, 2141
Dessart, L., Hillier, D. J., Li, C., & Woosley, S. 2012, MNRAS, 424, 2139
Dessart, L., Hillier, D. J., Woosley, S., et al. 2015, MNRAS, 453, 2189
Dessart, L., Hillier, D. J., Woosley, S., et al. 2016, MNRAS, 458, 1618
Ergon, M., Jerkstrand, A., Sollerman, J., et al. 2015, A&A, 580, A142
Ergon, M., Sollerman, J., Fraser, M., et al. 2014, A&A, 562, A17
Falk, S. W. & Arnett, W. D. 1977, ApJS, 33, 515
Hauschildt, P. H. & Baron, E. 1999, Journal of Computational and Applied Mathematics, 109, 41
Hillier, D. J. & Dessart, L. 2012, MNRAS, 424, 252
Hillier, D. J. & Miller, D. L. 1998, ApJ, 496, 407
Hubeny, I. & Mihalas, D. 2014, Theory of Stellar Atmospheres
Jerkstrand, A., Ergon, M., Smartt, S. J., et al. 2015, A&A, 573, A12
Jerkstrand, A., Fransson, C., & Kozma, C. 2011, A&A, 530, A45
Jerkstrand, A., Fransson, C., Maguire, K., et al. 2012, A&A, 546, A28
Kasen, D., Thomas, R. C., & Nugent, P. 2006, ApJ, 651, 366
Kerzendorf, W. E. & Sim, S. A. 2014, MNRAS, 440, 387
Kozma, C. & Fransson, C. 1992, ApJ, 390, 602
Kozma, C. & Fransson, C. 1998, ApJ, 496, 946
Kromer, M. & Sim, S. A. 2009, MNRAS, 398, 1809
Lucy, L. B. 1991, ApJ, 383, 308
Lucy, L. B. 1999, A&A, 345, 211
Lucy, L. B. 2002, A&A, 384, 725
Lucy, L. B. 2003, A&A, 403, 261
Lucy, L. B. 2005, A&A, 429, 19
Mazzali, P. A. 2000, A&A, 363, 705
Mazzali, P. A. & Lucy, L. B. 1993, A&A, 279, 447
Olson, G. L., Auer, L. H., & Buchler, J. R. 1986, J. Quant. Spec. Radiat. Transf., 35, 431
Paxton, B., Bildsten, L., Dotter, A., et al. 2011, ApJS, 192, 3
Paxton, B., Cantiello, M., Arras, P., et al. 2013, ApJS, 208, 4
Ross, S. 2007, Introduction to Probability Models
Scharmer, G. B. 1984, Accurate solutions to non-LTE problems using approximate lambda operators, ed. W. Kalkofen, 173–210
Shull, J. M. & van Steenberg, M. 1982, ApJS, 48, 95
Sobolev, V. V. 1957, Soviet Ast., 1, 678
Tanaka, M., Maeda, K., Mazzali, P. A., & Nomoto, K. 2007, ApJ, 668, L19
Verner, D. A., Ferland, G. J., Korista, K. T., & Yakovlev, D. G. 1996, ApJ, 465, 487
Verner, D. A. & Yakovlev, D. G. 1995, A&AS, 109, 125
Werner, K. & Husfeld, D. 1985, A&A, 148, 417
Woosley, S. E., Eastman, R. G., Weaver, T. A., & Pinto, P. A. 1994, ApJ, 429, 300
Woosley, S. E. & Heger, A. 2007, Phys. Rep., 442, 269

[2] www.nist.gov
[3] http://www.cfa.harvard.edu/amp/ampdata/kurucz23/sekur.html
[4] http://www.astronomy.ohio-state.edu/~nahar/_naharradiativeatomicdata/